Hybrid Manufacturing of Glass Using Femtosecond Machining

Nishan Khadka[1], Balark Tiwari[1], Todd Sparks[2], Robert G Landers[1], Edward C. Kinzel[1]
[1]Department of Aerospace and Mechanical Engineering, University of Notre Dame,
Notre Dame, IN 46556
[2]Product Innovation and Engineering, St. James, MO 65559

Abstract

Digital fabrication enables precise, flexible, and scalable manufacturing of intricate optical elements from traditional optics to complex microstructures and freeform optics. This paper presents a hybrid approach that combines filament-fed laser additive manufacturing with femtosecond laser micromachining to shape parts precisely. A framework for deterministically fabricating arbitrary features using a single-point machining basis is discussed. Using a 4-axis CNC stage, substrates are controlled relative to a CO_2 laser, locally heated to form optical elements, followed by surface mapping and registration for femtosecond laser micromachining.

1. Introduction

Precision optics is essential across a wide range of applications. The form complexity of optical lens geometries varies significantly depending on the intended use, ranging from rotationally symmetric aspheric lenses to freeform Alvarez lenses.[1] These lenses also demand stringent tolerances, with form accuracy often required to be below 50 nm and surface roughness under 1 nm for high-precision applications.[2] Commercial manufacturing techniques, such as single-point diamond turning, magneto-rheological finishing, or a combination of both, can achieve sub-wavelength ($\lambda/8$) form accuracy and sub-nanometer surface roughness.[2] However, for more complex geometries like aspheric lenses, fabrication typically involves a multi-step grinding and polishing process, which increases costs and extends production lead times.

Glass additive manufacturing has gained significant attention for its ability to produce complex glass structures.[3–6] One such method, Digital Glass Forming (DGF), has been explored for optics manufacturing.[3] This process involves selective laser heating of filament-fed glass relative to glass substrates, combined with CNC forming and shaping. DGF enables the creation of intricate shapes through precise path planning and layer-by-layer deposition, making it well-suited for fabricating optics with complex geometries.[4] During the process, glass is either reflowed in situ or post-processed to significantly reduce surface roughness to optical-grade levels.[3] However, a challenge arises as the reflow process often compromises the form accuracy of the optical components. This contrasts with subtractive manufacturing methods, which maintain high machining precision but are limited in handling complex geometries. Consequently, a hybrid approach is necessary to achieve both rapid fabrication and high precision in complex optical components.

Ultrafast laser machining is highly effective for fabricating micro-, nano-, and mesoscale features and bulk machining with nanometer precision.[7–11] The short pulse duration of ultrashort laser pulses allows for precise machining with minimal heat-affected zones (HAZ) [12] and is suitable for various materials, including silicate glasses used in optics. Femtosecond laser machining has been widely applied for direct glass processing in applications such as cleaving[13], microfluidics[14], waveguides[15], and optical components such as microlens

arrays[9,10]. It has also been used for bulk machining and fabrication of optical lenses[16][11]. There is ongoing research that aims to optimize process parameters for lens fabrication, making ultrafast laser machining a strong candidate for hybrid lens manufacturing[11,17,18].

This paper presents a hybrid manufacturing approach for glass, combining Digital Glass Forming (DGF) technology with ultrafast laser machining. Femtosecond laser machining is investigated to develop an effective set of basis functions for precise conformal machining of arbitrary surfaces. A single-point basis function is used to deterministically machine arbitrary shapes in unprocessed flat glass, while a hybrid framework is created that includes surface mapping, registration, and tool path generation to machine shapes in additively manufactured glass structures. The integration of femtosecond laser processing also expands the capabilities of hybrid manufacturing, enabling the production of functionalized optics such as Graded Index of Refraction (GRIN) optics and anti-reflection coated lenses through ultrafast texturing.

2. Micromachining Basis Functions

Femtosecond laser shots with pulse energy above the threshold fluence have finite material removal characterized spatially with shot width or diameter, *D,* and depth, *d*. Empirically determined basis functions for a single spot can be spatially arrayed to deterministically machine features on substrates. For a specific material and an ultrafast laser with a fixed wavelength and pulse duration, the basis function is influenced by control parameters: which are the laser spot size, *Ø,* Pulse energy, *E,* and the number of laser shots, *n* as explained in Equation 1. Non-linear effects (incubation effect) [18] of the Pulse Repetition Frequency (*PRF*) are ignored by carefully selecting PRF and *n* and only controlling the spatial array of the pulses.

$$(D,d) = f(\phi, E, n) \quad [1]$$

For laser shots with a Gaussian beam profile, the material removal creates holes with a Gaussian depth profile, as illustrated in Fig. 1. These single-point laser shots are referred to as 1-D cases. The micromachining basis function, described in Equation 1, can be applied to multiple shots, with depth (*d*) scaling linearly to create deeper holes. For 2-D cases, such as machining a single line, the 1-D basis function can be extended along a line. Here, the depth (*d*) is determined by the basis function, and the trench width is equivalent to the shot width (*D*). To maintain accurate spacing between laser shots when arrayed along a line, the linear scanning speed (*v*) and pulse repetition frequency (*PRF*) are adjusted to ensure that the total number of laser shots per spot matches the 1-D case. This is referred to as the equivalent pulse number [18], and in the 2-D case, it is denoted by $\bar{n}$, as defined in Equation 2.

$$\bar{n} = \frac{\phi \cdot PRF}{v} \quad [2]$$

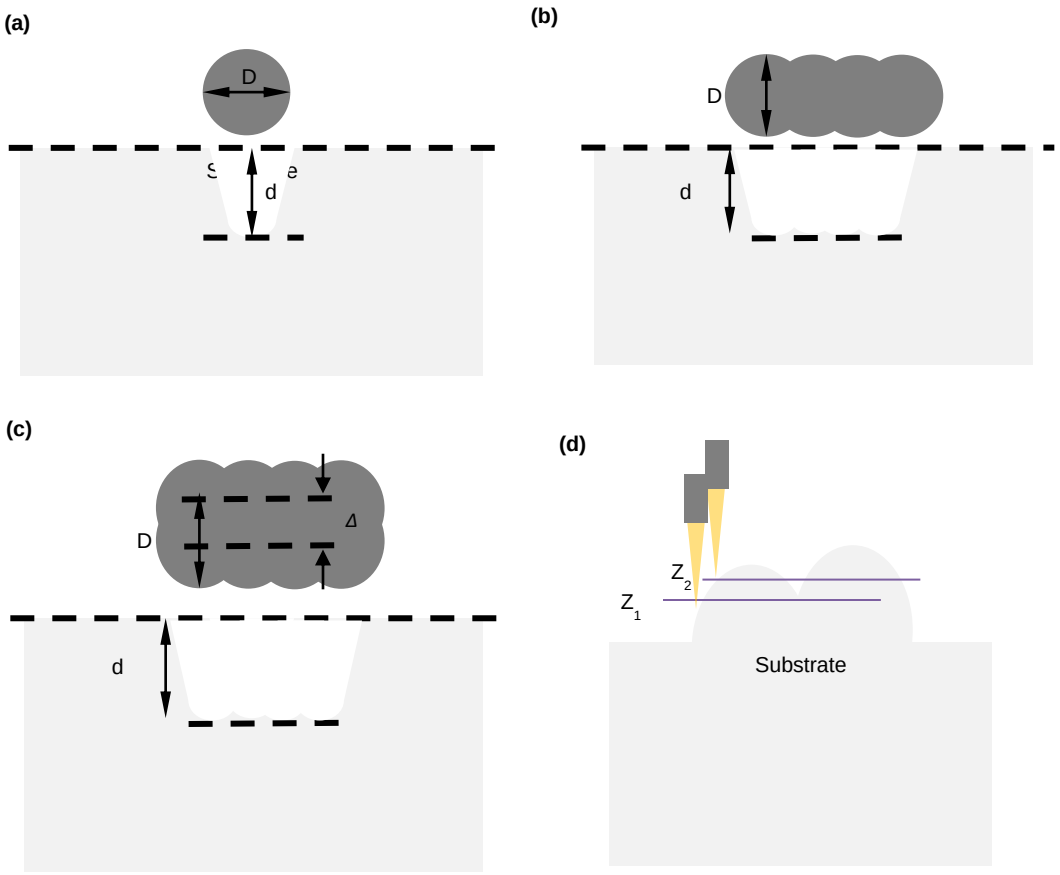

Fig. 1. Conceptual images illustrating ultrafast laser machining: (a) 1-D (holes), (b) 2-D (lines), (c) 3-D (trenches), and (d) conformal machining of curved profiles.

For 3-D machining or when processing large areas with dimensions exceeding those of individual laser shot craters, laser pulses need to be arranged along both the length and width of the feature. In this scenario, laser pulses are spaced along the length of the trench using *PRF* and scan speed (*v)* with each line of machining separated by hatch spacing (*Δ)*. To machine large trenches, a path of parallel lines or a raster scan can be utilized, with the equivalent pulse number, $\bar{n}$, adjusted according to Equation 3. For areas with arbitrary dimensions, machining can be performed using Equations 1 and 3, with the depth determined by Equation 1.

$$\bar{n} = \frac{\pi \cdot \phi^2 \cdot PRF}{4 \cdot v \cdot \Delta} \qquad [3]$$

For machining to arbitrary depths and conformal machining, the machining plane can be relocated to the bottom of the ablated crater after $\bar{n}$ laser shots and repeated until commanded depth is achieved. Conformal machining can be accomplished by following $\bar{n}$ in equation 3 for determining the equivalent number of shots and designing a path plan along the feature by point-to-point machining as shown conceptually in Fig 1d. This becomes analogous to traditional subtractive manufacturing processes such as milling.

3. Experimental Methods

3.1 Laser Processing Setup

A Pharos PH1-20W (Light Conversion, USA) maximum pulse energy of 200 μJ, and maximum pulse repetition frequency of 200 kHz was utilized for material processing. The laser operates at a central wavelength of 1030±5 nm and a pulse duration of 230 fs. The output beam was focused using a 5× near infrared (NIR) apochromat objective lens (Mitutoyo 378-802-6), resulting in a spot size of 11.6 μm at focus, determined by standard knife-edge measurements. A 4-axis CNC stages ANT130XY, ATS150, and ANTI130R from Aerotech was used for precision path planning against the laser pulses. An overhead visible camera is used to inspect the machining process. A schematic of the setup is shown in Fig. 2.

Fused silica substrates (25×75×1 mm) from AdValue Technologies, without additional processing, were used in this study.

The spatial profile of the machined features was assessed using a Zygo newView9000 white light interferometer, also without further processing.

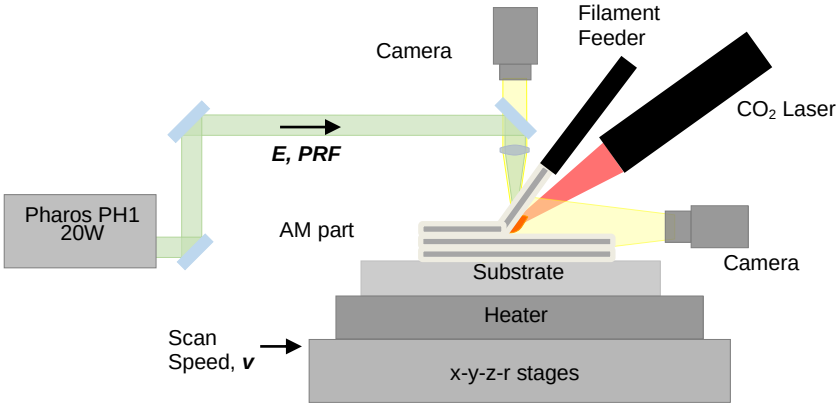

Fig. 2. Schematic of the laser processing setup with ultrafast laser processing and digital glass forming

3.2 Digital Glass Forming

For Digital Glass Forming, a CO_2 laser (λ = 10.6 μm) is focused on the machining plane of the femtosecond laser beam. The CO_2 laser is incident at a 30° angle relative to the horizontal and is used to heat and fuse glass filaments onto the substrate. A custom-designed filament feeder, incorporating an Aerotech stage, is used to feed cane filaments or optical fibers. The 4-axis CNC stages are employed for positioning and path planning of complex geometries. An in-plane visual camera is utilized to monitor the glass printing process. The CNC stages are equipped with a heat bed featuring 100W Watlow heaters to prevent thermal shock to the glass during deposition. 1 mm fused quartz filaments and SMF-28 telecom optical fiber were used in this study.

3.3 Hybrid Manufacturing Setup

The hybrid manufacturing system comprised digital glass fabrication to additively build geometries on fused quartz, followed by ex-situ imaging to resolve the surface profile of the printed parts and use the spatial information to machine them to the desired geometries. A VIEW

Benchmark metrology microscope was employed to map the spatial profile of the printed objects. Before scanning, a 3D scanning spray from AESUB was applied. The registration process, involving three steps after 3-D printing and before machining, is illustrated in Fig. 3.

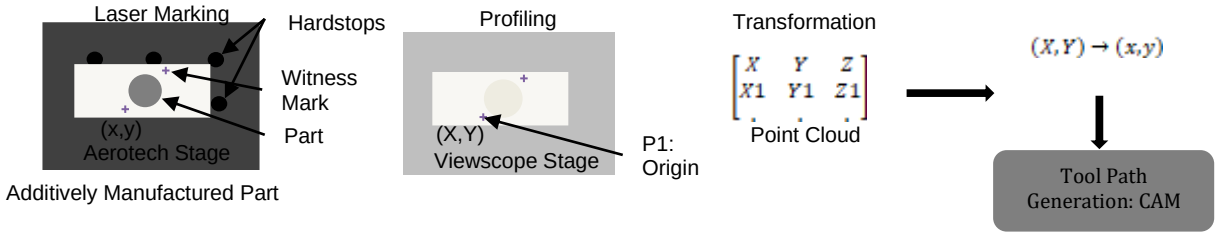

Fig. 3. Conceptual map of the co-ordinate transformation process during ex-situ imaging of the printed parts

Laser-machined witness marks were created after the digital glass-forming process. The substrates were aligned against hard stops to ensure consistent positioning. The part was then scanned relative to the witness marks using the view scope stages and repositioned in the machining setup. The (x, y) point cloud data from the Aerotech stages were derived from the (X, Y) point cloud information from the view stages using coordinate transformation. This data was then exported to custom-built CAM software for tool path generation.

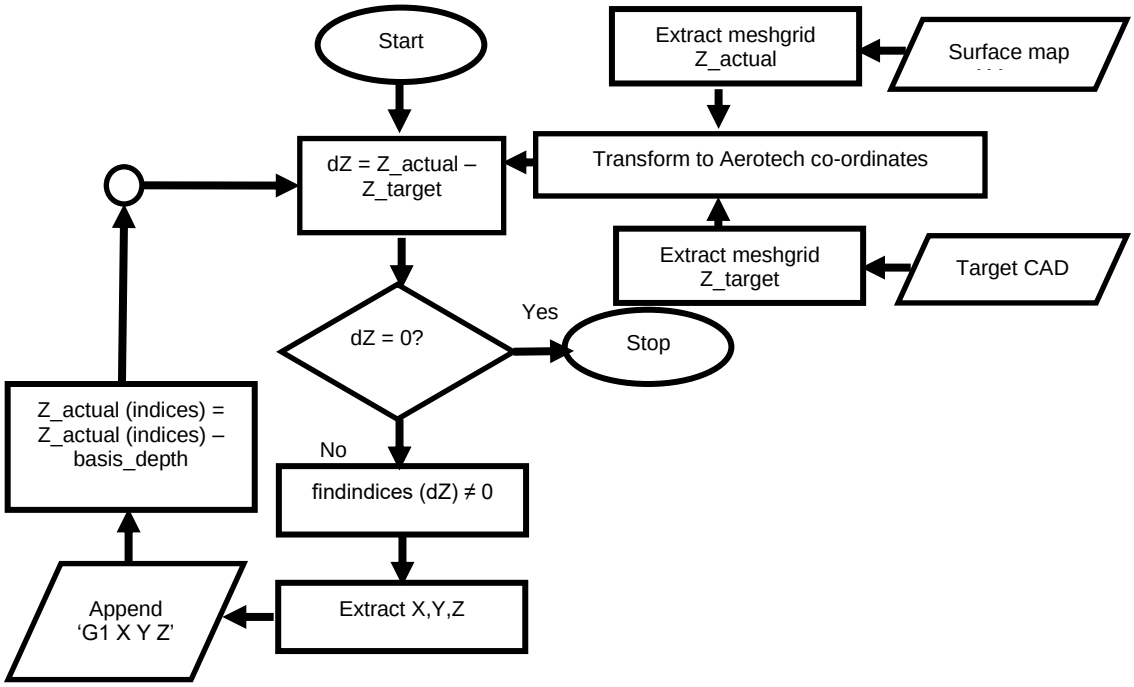

Fig. 4. Algorithm for tool path generation in the CAM software

The CAM software was developed using Python, based on a simple algorithm outlined in Fig. 4. The desired geometry was designed using SolidWorks 2021, and the spatial information was transformed into the Aerotech (x, y) coordinate system. The point cloud data was converted into a mesh and iteratively compared with the mapped printed part until the error between the two was zero. Point cloud information for the areas to be machined was extracted and

incorporated into G1 linear motion codes, maintaining $\bar{n}$, for a point-to-point machining path plan.

Fig. 5a. shows an example of a printed part mapped using a VIEW microscope, alongside the surface map of the ideal part. After processing with the CAM software, the tool path is generated to achieve the target profile, which is shown and highlighted in red in Fig. 5c. The final rendered surface map of the processed part is presented in Fig. 5d.

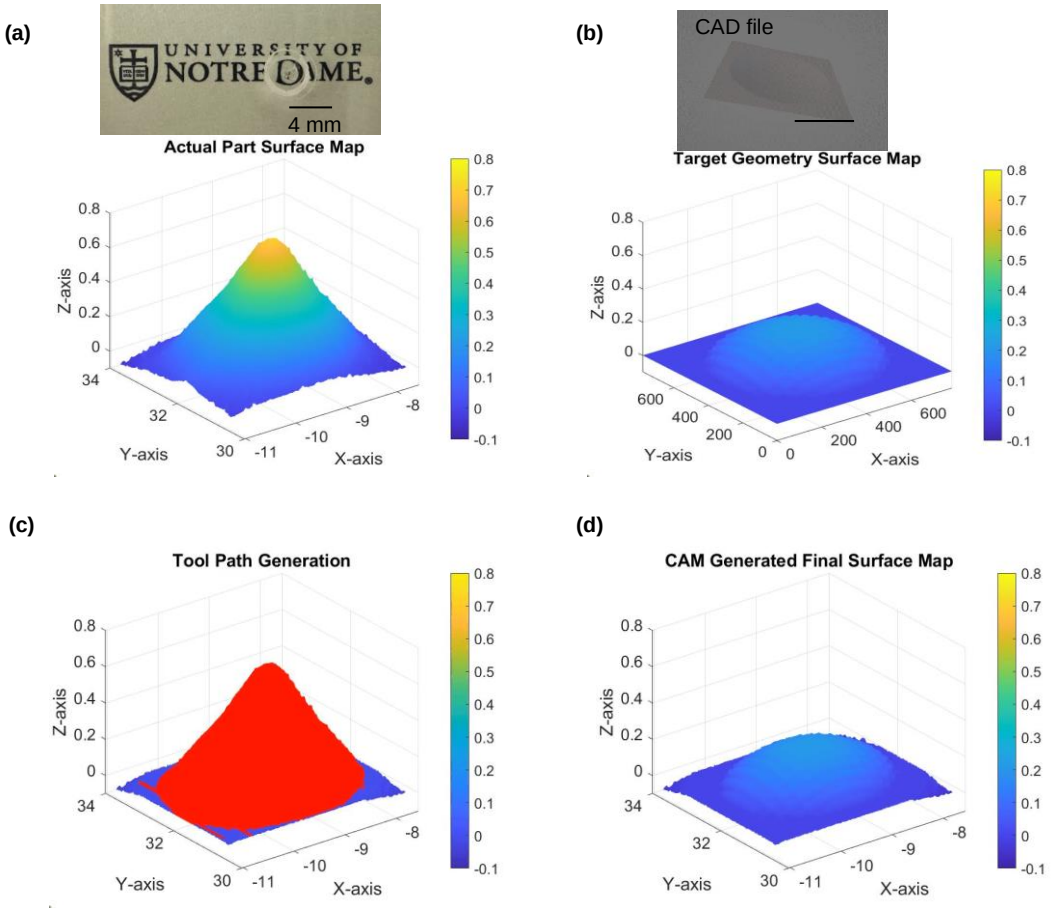

Fig. 5. (a) Photograph and surface map of the printed part, (b) 3-D image and surface map of the target geometry designed with CAD, (c) Surface map showing tool path coverage on the printed part, and (d) Surface map of the final part generated by CAM.

4. Results and Discussion

4.1 Mapping Micromachined Craters

The depth profile for laser-processed fused quartz was mapped as a function of pulse energy (E), with a focused laser beam of 11.57 μm. Using n =10 laser shots, the resulting holes were measured, and their cross-sections were plotted against pulse energy, as shown in Fig. 6a. The maximum diameter and depth of the machined holes are illustrated in Fig. 6b.

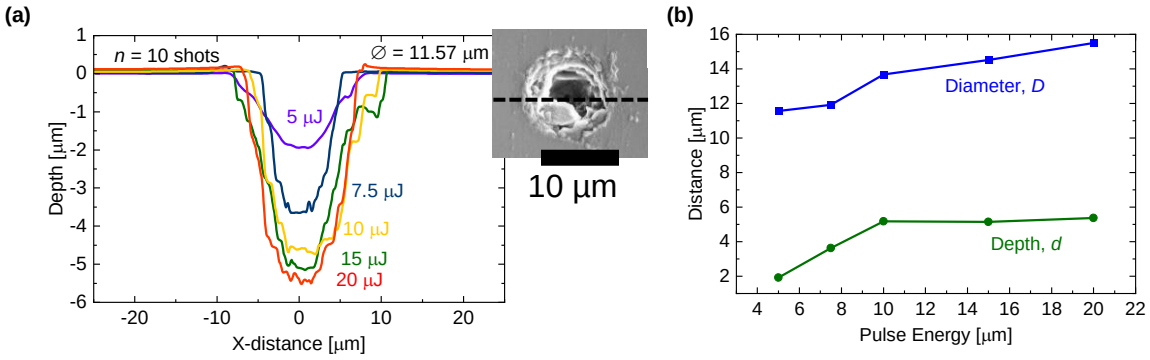

Fig. 6. (a) Cross-section of laser-processed holes at different pulse energies, and (b) Plot of depth and diameter as a function of pulse energy.

The depth and diameter of the machined craters increase with pulse energy. At high fluences, the total width of the craters saturates and approaches the width of the laser beam. Additionally, the depth of the craters logarithmically saturates at high fluences due to the effects of plasma formation in the air.

For a pulse energy of 5 µJ, the ideal Gaussian function fitted to n = 10 shots is depicted in Fig. 7a. The linearity of the 5 µJ pulse energy was quantified for n shots, and this is shown in Fig. 7b as a function of the number of shots.

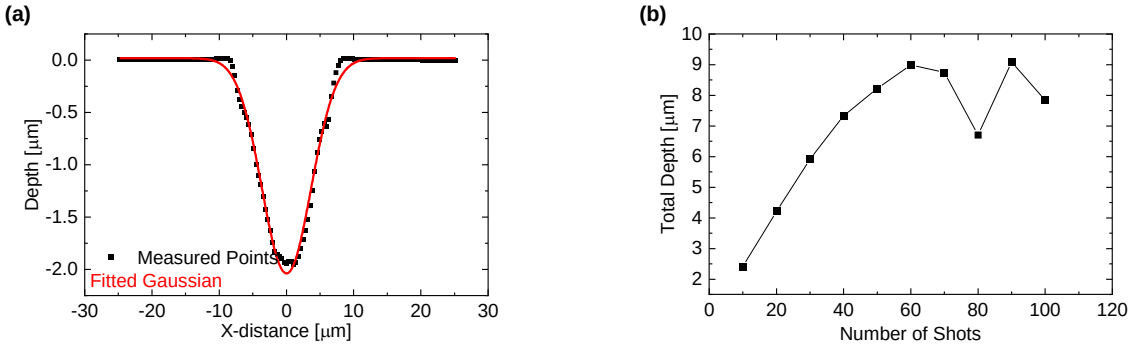

Fig. 7. (a) Cross-section of the micromachined crater fitted with a Gaussian function, and (b) Uncertainty in depth and diameter of the machined craters from 50 samples.

The fitted Gaussian function is described by Equation [4]. For the 5 µJ pulse energy, the uncertainty in crater depth was measured to be ±0.39 µm, and the uncertainty in diameter was ±2.44 µm.

$$d = -2.05 \cdot \exp\left[-\left(\frac{x - 0.019}{7.2912}\right)^2\right] \qquad [4]$$

According to Fig. 7b, the micromachined crater depth scales linearly with the number of shots up to 40, with the depth being n times the 5 µJ basis function. Beyond 40 shots, the depth scales non-linearly due to the taper angle of the machined craters, which makes it increasingly difficult to ablate and remove material at greater depths. Nevertheless, the linear relationship of crater depth up to 40 shots allows for deterministic machining of features by arraying 40 shots simultaneously on a plane.

4.2 Subtractive Machining: 2-D, 3-D and Conformal

The 5 µJ micromachining basis function was extended to 2-D (machining lines) and 3-D (machining trenches) with an equivalent pulse number of 40 shots, as set by Equation 3. For machining lines, a pulse repetition frequency (*PRF*) of 20 kHz and a scanning speed (*v*) of 5.3 mm/s were used. For machining trenches, a *PRF* of 20 kHz and a scanning speed of 11.25 mm/s were employed, with 60% overlap between machining lines to achieve a net $\bar{n}$ of 40 shots per spot. Fig. 8a shows the surface map and cross-section of the machined line, while Fig. 8b presents the surface map and cross-section of the machined trench. These results were compared to the convolution of the ideal Gaussian basis function.

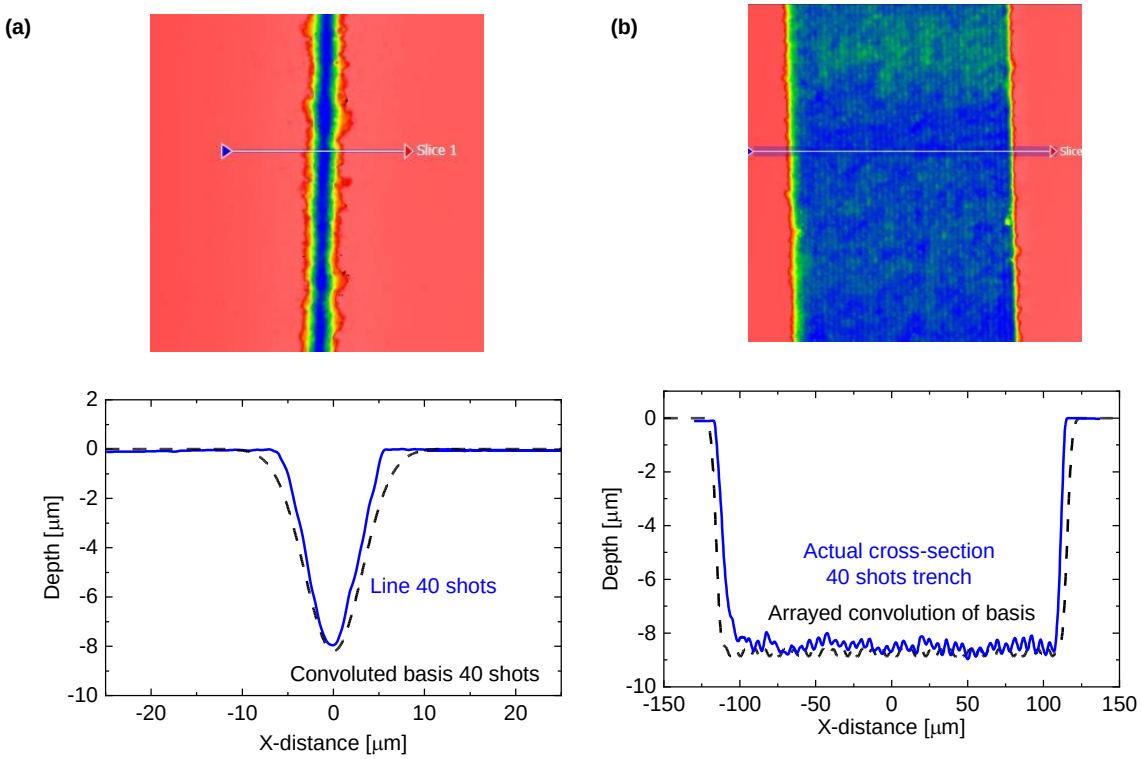

Fig. 8. Surface map and cross-section of a micromachined: (a) line and (b) trench, both machined to a commanded depth of 8 µm.

Maximum error of 2.3 µm in diameter and an error in depth of 0.17 µm seen for the micromachined line without correcting for the uncertainty in basis functions. For the trench 2 µm error in the width of the track and a 0.25 µm error in the depth was seen which were also below the uncertainty for the basis functions. Using this framework, a 4-leaf clover was fabricated on bare glass to an expected depth of 250 µm by changing the machining plane after 40 shots. This is shown in Fig 9. An average error of 120 nm was observed in the area highlighted in Fig 8a.

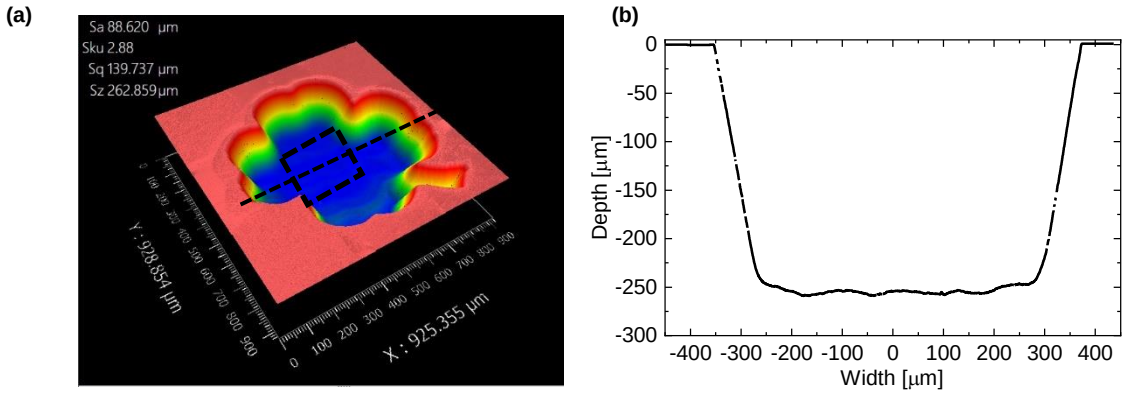

Fig 9 a. Surface map and b. the cross-section of a micromachined 4-leaf clover to a depth of 250 µm

4.2 Subtractive Manufacturing Conformal Surface

The CAM software generated tool paths for machining a stepped sphere, as depicted in Fig. 10a, which was designed with CAD. The part has a total depth of 100 µm and a diameter of approximately 1 mm. The 5 µJ micromachining basis was used to machine out approximately 8 µm depth with 40 shots on a single plane.

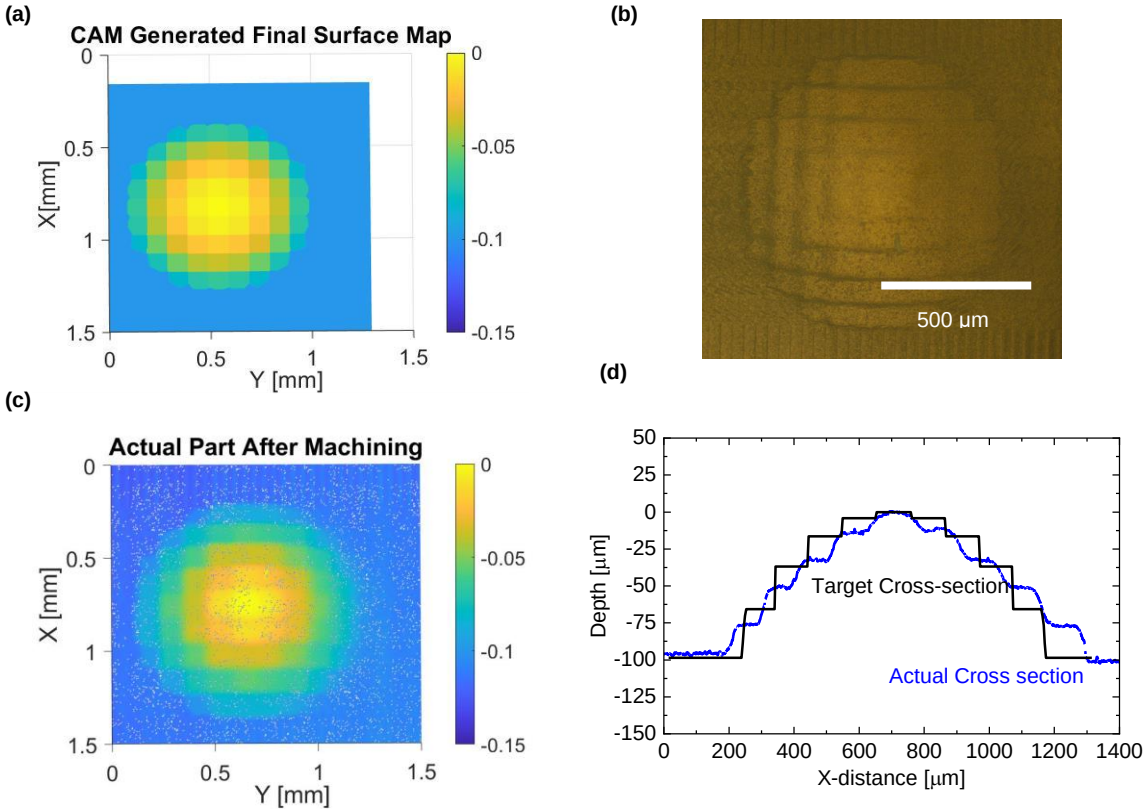

Fig. 10. (a) Surface map of the stepped spherical profile rendered using CAM, (b) Optical microscope image of the machined profile on fused silica, (c) Surface map of the actual part after machining, and (d) Comparison of the cross-section of the ideal part versus the machined part along the diameter of the stepped spherical profile.

The machining plane was then adjusted and the process repeated until the desired depth was achieved. Fig. 10b shows a microscopic image of the machined profile, and Fig. 10c displays the surface map of the part after applying a 3-D scanning spray and imaging with the metrology microscope.

A comparison between the actual cross-section and the target cross-section of the feature demonstrates good agreement at both the peak and base of the desired profile. However, along the X-Y axis of the profile, significant deviations (~100 μm) were observed due to the convolution of the Gaussian basis function and the resulting taper along the profile. Despite these deviations, the comparison of depth revealed a maximum error of 1.32 μm, with an average error of less than 100 nm.

4.3 Hybrid Manufacturing Artifact

Using Digital Glass Forming (DGF), 1 mm fused quartz cane filaments were employed to fabricate dense walls on 5×10×2 mm³ fused quartz substrates, as shown in Fig. 11a and 11b. The structure was printed at 70W with a CO_2 laser beam diameter ($Ø_{CO2}$) of 1.5 mm (FWHM) at a speed of 2 mm/s, with a feed-to-speed ratio (f/v) of 1.0. A spacing of 1.15 mm was maintained between the walls, with two layers printed, the second layer separated by 0.575 mm. The surface map of the fabricated walls is depicted in Fig. 11a.

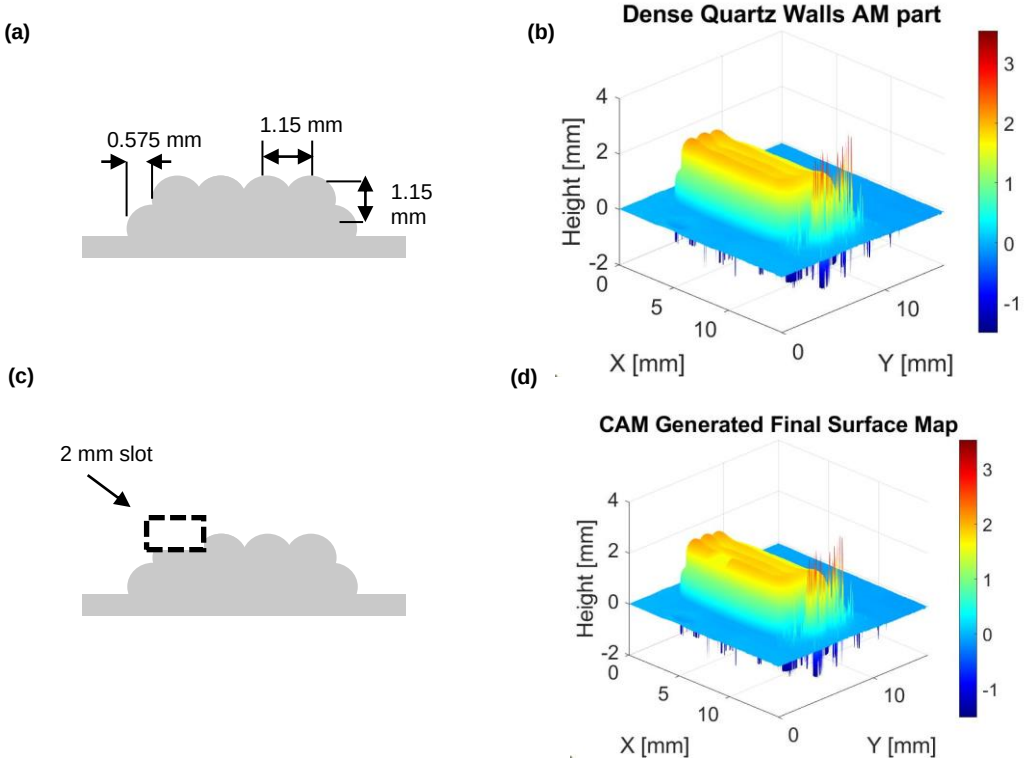

Fig. 11. (a) Diagram highlighting the fabrication of dense fused quartz walls, (b) Surface map of the fabricated quartz walls, (c) Target geometry with a 2 mm slot, and (d) CAM-generated surface map of the final geometry.

For the target geometry, a 2 mm slot with approximately 300 μm depth on the printed beads was desired. The CAM-generated final surface map is shown in Fig. 11d. Using the 5 μJ basis function and machining 40 shots on a single plane, the CAM-generated tool path was implemented, and the final image after machining is depicted in Fig. 12a.

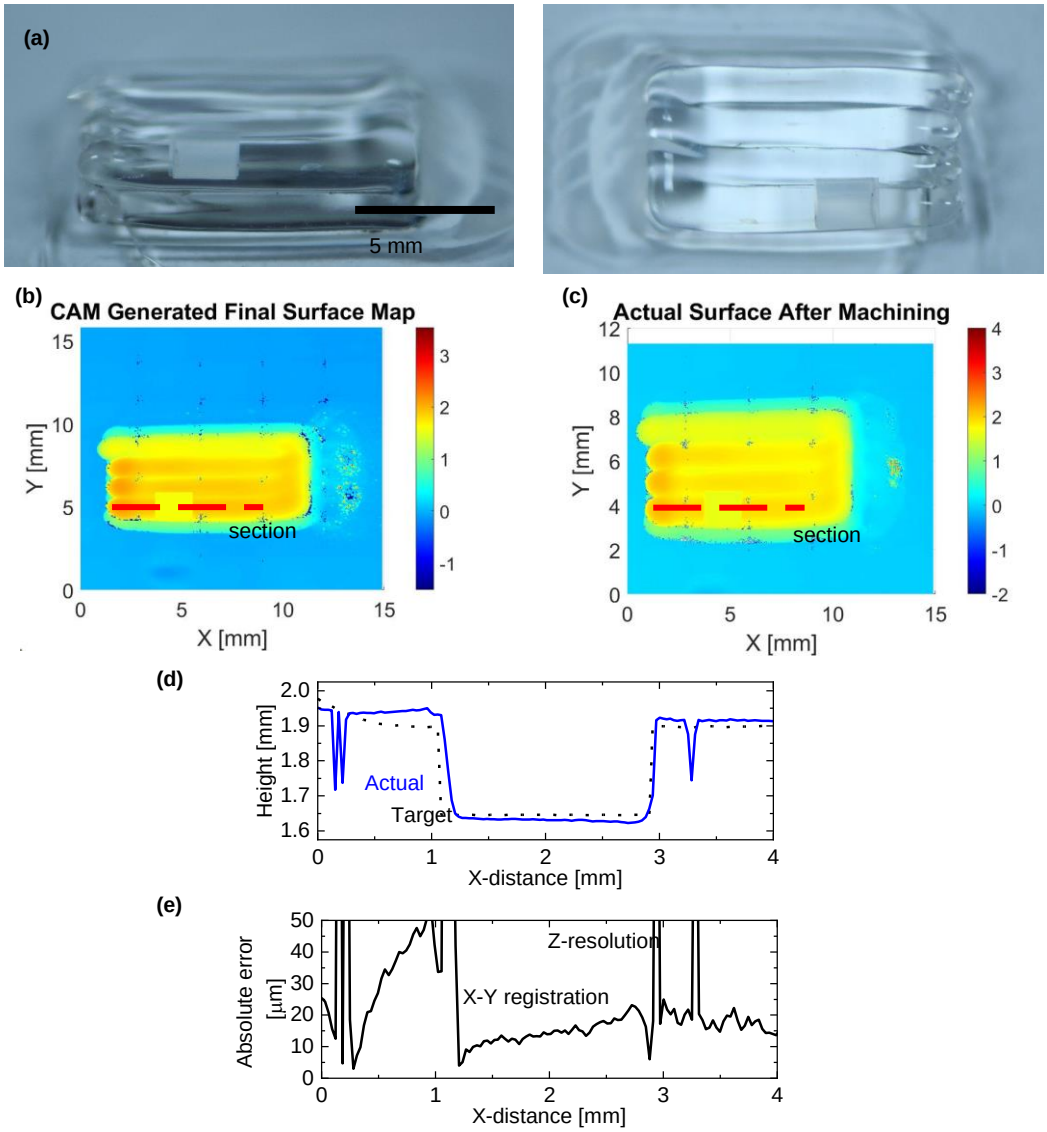

Fig. 12. (a) Photographs of the hybrid-manufactured part on fused quartz. Comparison of surface maps: (b) CAM-generated final map, (c) actual map after machining, (d) comparison of the cross-sections of target versus actual, and (e) plot of absolute error along the length of the section.

Fig. 12b shows a comparison between the surface map of the ideal part generated using CAM and the actual surface map after machining. Fig. 12d presents a cross-section of the surface map, demonstrating that the actual part closely follows the intended path. Fig. 12e highlights the absolute error along the length of the section, revealing significant depth errors up to 10 μm and sharp peaks exceeding 100 μm at different locations, particularly at the beginning and end of the profile. These discrepancies are attributed to X-Y registration errors during coordinate transformation between the machining plane and the imaging plane. The low-frequency peaks observed in Fig. 12e are due to Z-resolution errors, constrained by the resolution of the metrology microscope. Improved in-situ imaging and tool path generation with nanometer-level resolution could enhance hybrid machining accuracy.

5. Conclusions

Precision fabrication of optical lenses often requires hybrid approaches that combine the high precision of subtractive manufacturing with the complex form factor capabilities of additive processes, such as Digital Glass Forming (DGF). This hybrid methodology enhances cost-efficiency and throughput for producing complex optical lenses. Ultrafast laser machining is a suitable tool with its high precision and compatibility with laser additive manufacturing such as digital glass forming. Femtosecond laser machining was modeled using single point basis functions, showing linear depth scaling up to 40 shots with 5 μJ pulse energy, achieving sub-100 nm precision for machining arbitrary shapes to deterministic depths in fused quartz. However, Gaussian basis function convolution caused tapering and precision loss in the X-Y dimensions. An in-house CAM software was employed for tool path generation with a 2-step ex-situ imaging and machining hybrid framework. Hybrid manufacturing agreed with the commanded machining path but revealed X-Y registration errors impacting precision to within 10 μm. Future improvements with in-situ imaging and refined tool path generation could achieve sub-50 nm accuracy. This integration also opens possibilities for hybrid manufacturing of advanced optics, such as anti-reflective lenses and graded index of refraction (GRIN) optics.

6. Acknowledgement

This work was supported by Product Innovation and Engineering (PINE) and the US Naval Air Command (NAVAIR) SBIR (N6893621C0048). We would also like to acknowledge Zygo Corp. for their support with instrumentation.

7. References

1. J. Babington, "Alvarez lens systems: theory and applications," Opt. Syst. Des. 2015 Opt. Des. Eng. VI **9626**, 962615 (2015).
2. A. Drouin, P. Lorre, J.-S. Boisvert, S. Loranger, V. L. Iezzi, and R. Kashyap, "Spatially resolved cross-sectional refractive index profile of fs laser–written waveguides using a genetic algorithm," Opt. Express **27**(3), 2488 (2019).
3. J. Luo, L. J. Gilbert, D. A. Bristow, R. G. Landers, J. T. Goldstein, A. M. Urbas, and E. C. Kinzel, "Additive manufacturing of glass for optical applications," Laser 3D Manuf. III **9738**, 97380Y (2016).
4. J. Luo, H. Pan, and E. C. Kinzel, "Additive Manufacturing of Glass," J. Manuf. Sci. Eng. Trans. ASME **136**(6), 1–6 (2014).
5. K. Sasan, A. Lange, T. D. Yee, N. Dudukovic, D. T. Nguyen, M. A. Johnson, O. D. Herrera, J. H. Yoo, A. M. Sawvel, M. E. Ellis, C. M. Mah, R. Ryerson, L. L. Wong, T. Suratwala, J. F. Destino, and R. Dylla-Spears, "Additive Manufacturing of Optical Quality Germania-Silica Glasses," ACS Appl. Mater. Interfaces **12**(5), 6736–6741 (2020).
6. Y. Zhu, T. Tang, S. Zhao, D. Joralmon, Z. Poit, B. Ahire, S. Keshav, A. R. Raje, J. Blair, Z. Zhang, and X. Li, "Recent advancements and applications in 3D printing of functional optics," Addit. Manuf. **52**(November 2021), 102682 (2022).
7. N. Khadka, Y. Yang, A. Hoffman, M. Rosenberger, and E. C. Kinzel, "Spectral selectivity and blackening through direct-write femtosecond micromachining," **12878**, 20 (2024).
8. N. Khadka, Y. Yang, J. Haug, M. Palei, M. Rosenberger, A. Hoffman, and E. Kinzel, "Ultrafast Laser Texturing of Metal Surfaces: Effects of Process Parameters on Surface Reflectance and Possibility of Hierarchical Structuring," (2022).
9. S. Schwarz, S. Rung, C. Esen, and R. Hellmann, "Rapid fabrication of precise glass

axicon arrays by an all laser-based manufacturing technology," J. Laser Appl. **32**(1), (2020).
10. T. Fricke-Begemann, J. Li, J. Ihlemann, P. R. Herman, and G. Marowsky, "Micro-lens machining on optical fibers by direct laser ablation," Photonics North 2004 Photonic Appl. Astron. Biomed. Imaging, Mater. Process. Educ. **5578**(December 2004), 589 (2004).
11. C. K. Ng, C. Chen, Y. Yang, F. Zhang, B. F. Ju, and Y. L. Chen, "Femtosecond laser micro-machining of three-dimensional surface profiles on flat single crystal sapphire," Opt. Laser Technol. **170**(September 2023), 110205 (2024).
12. S. M. Eaton, H. Zhang, P. R. Herman, F. Yoshino, L. Shah, J. Bovatsek, and A. Y. Arai, "Heat accumulation effects in femtosecond laser-written waveguides with variable repetition rate," Opt. Express **13**(12), 4708 (2005).
13. M. A. Al Mamun, P. J. Cadusch, T. Katkus, S. Juodkazis, and P. R. Stoddart, "Quantifying end-face quality of cleaved fibers: Femtosecond laser versus mechanical scribing," Opt. Laser Technol. **141**(February), 107111 (2021).
14. J. Yu, J. Xu, Q. Dong, J. Qi, J. Chen, A. Zhang, Y. Song, W. Chen, and Y. Cheng, "Low-loss optofluidic waveguides in fused silica enabled by spatially shaped femtosecond laser assisted etching combined with carbon dioxide laser irradiation," Opt. Laser Technol. **158**(PA), 108889 (2023).
15. F. Chen and J. R. V. de Aldana, "Optical waveguides in crystalline dielectric materials produced by femtosecond-laser micromachining," Laser Photonics Rev. **8**(2), 251–275 (2014).
16. S. Schwarz, G.-L. Roth, S. Rung, C. Esen, and R. Hellmann, "Fabrication and evaluation of negative axicons for ultrashort pulsed laser applications," Opt. Express **28**(18), 26207 (2020).
17. W. Wang, J. Chen, D. Li, D. Feng, and Y. Tu, "Modelling and optimisation of a femtosecond laser micro-machining process for micro-hole array products," Int. J. Adv. Manuf. Technol. **82**(5–8), 1293–1303 (2016).
18. K. Liao, W. Wang, X. Mei, W. Tian, H. Yuan, M. Wang, and B. Wang, "Shape regulation of tapered microchannels in silica glass ablated by femtosecond laser with theoretical modeling and machine learning," J. Intell. Manuf. **34**(7), 2907–2924 (2023).